The Astrophysical Journal, 929:85 (11pp), 2022 April 10 https://doi.org/10.3847/1538-4357/ac4fbe

A Partial Filament Eruption in Three Steps Induced by External Magnetic Reconnection

Jun Dai[1,2], Zhentong Li[1,2], Ya Wang[1,2], Zhe Xu[1,2], Yanjie Zhang[1,2], Leping Li[3,4], Qingmin Zhang[1,2], Yingna Su[1,2], and Haisheng Ji[1,2]
[1] Key Laboratory of Dark Matter and Space Astronomy, Purple Mountain Observatory, CAS, Nanjing, 210008, People's Republic of China; daijun@pmo.ac.cn
[2] School of Astronomy and Space Science, University of Science and Technology of China, Hefei, 230026, People's Republic of China
[3] Key Laboratory of Solar Activity, National Astronomical Observatories, CAS, Beijing 100101, People's Republic of China
[4] School of Astronomy and Space Science, University of Chinese Academy of Sciences, Beijing 100049, People's Republic of China
Received 2021 November 2; revised 2022 January 21; accepted 2022 January 24; published 2022 April 15

Abstract

We present an investigation of partial filament eruption on 2012 June 17 in the active region NOAA 11504. For the first time, we observed the vertical splitting process during the partial eruption with high-resolution narrowband images at 10830 Å. The active filament was rooted in a small δ-sunspot of the active region. Particularly, it underwent the partial eruption in three steps, i.e., the precursor, the first eruption, and the second eruption, while the latter two were associated with a C1.0 flare and a C3.9 flare, respectively. During the precursor, slow magnetic reconnection took place between the filament and the adjoining loops that also rooted in the δ-sunspot. The continuous reconnection not only caused the filament to split into three groups of threads vertically but also formed a new filament, which was growing and accompanied brightening took place around the site. Subsequently, the growing filament erupted together with one group splitted threads, resulted in the first eruption. At the beginning of the first eruption, a subsequent magnetic reconnection occurred between the erupting splitted threads and another ambient magnetic loop. After about 3 minutes, the second eruption occurred as a result of the eruption of two larger unstable filaments induced by the magnetic reconnection. The high-resolution observation provides a direct evidence that magnetic reconnection between filament and its ambient magnetic fields could induce the vertical splitting of the filament, resulting in partial eruption.

Unified Astronomy Thesaurus concepts: Solar active region filaments (1977); Solar filaments (1495); Solar filament eruptions (1981); Magnetic fields (994); Solar magnetic reconnection (1504); Solar active region magnetic fields (1975)

Supporting material: animations

1. Introduction

Solar filaments are defined as the structural feature of full cool and dense plasma suspended in the solar corona (Engvold 1998; Labrosse et al. 2010; Mackay et al. 2010; Régnier et al. 2011; Parenti 2014; Karpen 2015; Gibson 2018), which are located along the magnetic polarity inversion lines (PILs) in the photosphere (van Ballegooijen & Martens 1989; Martin 1998; Parenti 2014; Gibson 2018). High-resolution Hα observations have confirmed that filaments are composed of highly dynamic fine-scale threads (Chae et al. 2000; Lin et al. 2005, 2008; Schmieder et al. 2010; Berger 2014). The limb quiescent prominence threads appear to be long thick and predominately quasi-vertical (Berger & Haerendel 2009; Haerendel & Berger 2011), while the active filaments, located adjacent to the sunspots (Engvold 2015), appear to be long thin and relatively horizontal (Okamoto et al. 2007), which may represent thin magnetic strings (Lin et al. 2005).

Generally, changes in the magnetic field topology of filaments can trigger eruptions, which include tether cutting (TC; Moore et al. 2001) or flux cancellation (van Ballegooijen & Martens 1989), emerging magnetic flux (Chen & Shibata 2000), and magnetic flux injection (Chen 1996). Moreover, highly dynamic filaments can be eruptive due to the ideal magnetohydrodynamic (MHD) instabilities, including torus instability (Kliem and Török 2006) and ideal kink instability (Hood & Priest 1981; Török et al. 2004). Typically, filament eruptions are preceded by their precursor activities (Chen 2011), such as darkening and widening (Martin 1980), reconnection-favored emerging flux (Feynman & Martin 1995), large-amplitude oscillation (Chen et al. 2008; Zhang et al. 2012), heating and particle acceleration (Hernandez-Perez et al. 2019), and soft X-ray (SXR) brightening (Mitra et al. 2020). In addition, EUV or chromosphere brightenings inside the filament or its close vicinity are also considered as precursors (Sterling & Moore 2005; Alexander et al. 2006; Sterling et al. 2011; Yan et al. 2013; Wang et al. 2018; Devi et al. 2020).

However, filament eruptions can be a failed (Ji et al. 2003; Liu et al. 2009; Dai et al. 2021) result from strong enough overlying magnetic fields (Török and Kliem 2005) or the lack of gained energy (Shen et al. 2011). The difference between full and failed eruptions is whether the filament mass and magnetic structure completely escaped the Sun, producing coronal mass ejections (CMEs; e.g., Dai et al. 2018), or not having escaped at all. Occasionally, after experiencing a failed eruption and stopping at a certain height for hours, a filament would continue to erupt successfully, i.e., so-called two step or multi-site eruptions (Byrne et al. 2014; Gosain et al. 2016; Chandra et al. 2017; Filippov 2018). In addition, there is a kind of filament eruption called partial eruption (Gilbert et al. 2007). In partial eruptions, filaments usually split into two parts with one part being fully erupted and the other remaining (Gilbert et al. 2000; Liu et al. 2007; Shen et al. 2012; Zheng et al. 2017; Cheng et al. 2018; Wang et al. 2020; Yang et al. 2020).

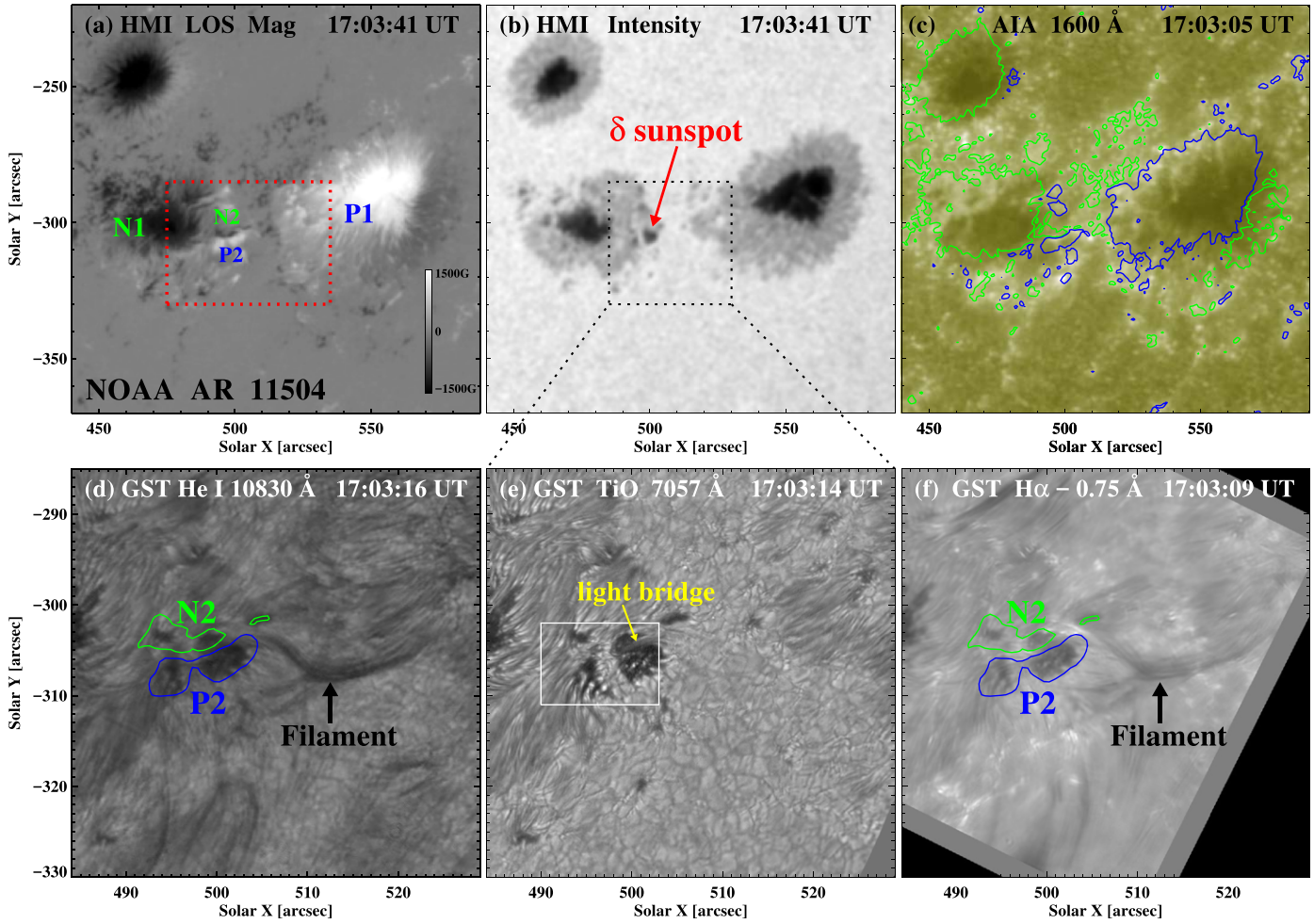

Figure 1. Overview of AR 11504 including the filament and the δ sunspot. Panels (a)–(c) provide an LOS magnetogram and an intensity image observed by HMI and a UV image in 1600 Å observed by AIA. Panels (d)–(f) show enlarged images from the boxed area in panel (b) of He I 10830 Å, TiO 7057 Å, and the Hα blue wing observed by GST. The red dotted rectangle in (a) shows the FOV of Figure 3 and Figures 4(a)–(f). The negative and positive magnetic fields of sunspots are denoted by N1, N2, P1, and P2 in panel (a). The green and blue contours in (c) represent the negative and positive magnetic fields with the magnetic strengths of −200 and 200 G. The negative and positive parts of the δ sunspot are denoted by green and blue contours with the magnetic strengths of −250 and 450 G in panels (d) and (f). The total flux of 10830 Å and TiO intensity, and the total positive and negative magnetic fluxes within the white box in (e) are calculated, and their temporal profiles are plotted in Figures 2(b)–(c).

Typically, graphic models (Gilbert et al. 2001) and three-dimensional MHD simulations (Gibson & Fan 2006) have found that the magnetic reconnection within a filament leads to vertical splitting of the filament, and EUV brightening can be detected at the splitting location (Tripathi et al. 2009; Shen et al. 2012; Tripathi et al. 2013; Zhang et al. 2015; Cheng et al. 2018). Meanwhile, through MHD simulations Birn et al. 2006 suggested another mechanism called nonuniform magnetic twist. Since a flux rope exists in places with different magnetic helicities, the twist of one part reaches kink instability and thus splits out and runs away, while the remaining part will have a low twist (Bi et al. 2015). Recently, Liu et al. 2012 found that partial eruptions can occur within double-decker filaments, and only the upper filament erupted after being activated due to magnetic flux and current changes or the occurrence of magnetic reconnection (Liu et al. 2012; Kliem et al. 2014; Zheng et al. 2019; Pan et al. 2021).

Furthermore, by analyzing the 3D magnetic configuration of a partial eruption, Zhang et al. (2015) found that the runaway material may escape along the surrounding open magnetic fields, which suggests that magnetic structures around the filaments is also an influential factor in the partial eruption. Chen et al. (2018) reported that a filament splits into three parts on its ascent due to the TC reconnection below the middle of the filament, and only the middle high-lying part erupted. More recently, Monga et al. (2021) highlighted that the reconnection process between the filament magnetic field and its ambient loops can induce the splitting of the filament, which is supported by similar results from high-resolution observation (Li et al. 2016; Xue et al. 2016). These studies have provided new constraints to partial filament eruptions, but the specific mechanisms still need more detailed analysis.

On 2012 June 17, a partial filament eruption occurred in AR 11504 and was well recorded with He I 10830 Å narrowband images by the Goode Solar Telescope (GST) at the Big Bear Solar Observatory (BBSO). This high-resolution observation gives us a good opportunity to analyze and understand the mechanisms of partial eruptions. Particularly, the filament underwent partial eruption in three steps, which was associated with two C-class flares and multiple hot channels. Zeng et al. (2014) have reported the excitation of He I atoms by EUV illumination by analyzing the emission flux of the flares from the

corona to the transition region and then to the chromosphere. In this paper, we focus on the triggering process and dynamic behavior of the partial eruption. The observation and data analysis are described in Section 2. The results are presented in Section 3. A detailed interpretation and discussion are presented in Section 4 and a brief summary is given in Section 5.

2. Observation and Data Analysis

The New Solar Telescope is a 1.6 m aperture ground-based off-axis telescope at BBSO (Goode et al. 2010), which was renamed the GST in 2017 July. Since the off-axis design was removed from the central obscuration, GST can significantly reduce stray light, and the long duration of good seeing conditions combined with a high-order adaptive optics system enable providing consecutive observations for solar activities with diffraction-limited images (Cao et al. 2010). On 2012 June 17, from 17:01–18:08 UT, GST pointed to the active region NOAA 11504, targeting a small active filament. High-resolution filtergrams were obtained in narrowband Lyot filters in the He I 10830 Å blue wing (0.25 Å, bandpass: 0.5 Å) and in Hα 6563 Å blue wing (−0.75 Å, bandpass: 0.25 Å), and also in a broadband filter (bandpass: 10 Å) containing the TiO 7057 Å line. The 10830 Å data were acquired by employing a high sensitivity HgCdTe CMOS IR focal plane array camera (Cao et al. 2010), with a cadence of 10 s, pixel size of 0.″0875 with a field of view (FOV) of 90″ × 90″. The Hα image scale is 0.″03 pixel^{-1} and has a cadence of 30 s, with a FOV of 60″ × 60″. The TiO images have a spatial sampling and time cadence of 0.″0375 pixel^{-1} and 30 s, respectively, with a FOV of 70″ × 70″.

Full-disk photospheric continuum intensity images and line-of-sight (LOS) magnetograms were observed by the Helioseismic and Magnetic Imager (HMI; Schou et al. 2012) on board the Solar Dynamics Observatory (SDO; Pesnell et al. 2012) with a spatial resolution of 1.″2 and time cadence of 45 s. HMI also provides continuous vector magnetic fields (Turmon et al. 2010) in the HMI Active Region Patches region. In addition, we employ UV and EUV images from the Atmospheric Imaging Assembly (AIA; Lemen et al. 2012) on board SDO. For level 1.5 AIA images, their spatial sampling is fixed at 0.″6 pixel^{-1} and have a time cadence of 12 s. The level_1 data from AIA and HMI were calibrated using the standard Solar SoftWare programs `aia_prep.pro` and `hmi_prep.pro`, respectively. SXR light curves of the flare were recorded by the GOES spacecraft with a cadence of 2 s. The associated CMEs were observed by the C2 on board the SOHO Large Angle and Spectrometric Coronagraph (LASCO; Brueckner et al. 1995).

The two large sunspots and the small δ sunspot are recognizable in HMI intensity images, which are very helpful for a convincing co-alignment between the local TiO and full-disk intensity images. The HMI intensity and TiO images were co-aligned by carrying out an automatic mapping approach developed by Ji et al. (2019). Visual inspections and error corrections were made during the co-alignment, and we estimate the accuracy to be within 0.″5.

In order to reconstruct the coronal magnetic fields before eruptions in AR 11504, we apply the nonlinear force-free field (NLFFF; Wiegelmann et al. 2006, 2012) model using the magneto-frictional method (Guo et al. 2016), which is implemented in Message Passing Interface Adaptive Mesh Refinement Versatile Advection Code (Keppens et al. 2003, 2012; Porth et al. 2014). The calculation is performed within a box of 288 × 170 × 170 uniform grid points, which almost covers the whole active region.

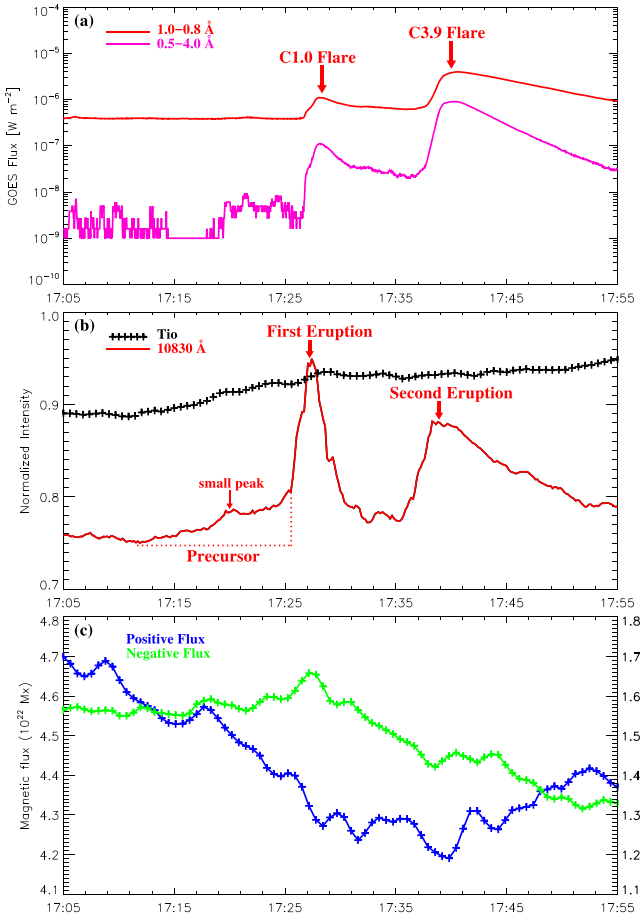

Figure 2. (a) SXR light curves of the two flares in 1–8 Å (red line) and 0.5–4 Å (magenta line). (b) Light curves (normalized) in 10830 Å and TiO within the white box of Figure 1(e). (c) Temporal evolutions of the total positive and negative magnetic fluxes within the white box of Figure 1(e). An animation showing the light curves and magnetic flux in the delta sunspot region in panels (b) and (c) is available. These are show on the right side of the animation. The left side of the animation shows the He I 10830 Å (top; see also panels (a1)–(a4) of Figure 3), TiO (middle), and LOS-mag (bottom) images. The animation real-time duration is 12 s, which covers 50 minutes starting at 17:05 UT and ending the same day at 17:55 UT.

(An animation of this figure is available.)

3. Result

3.1. Overview

As shown in Figures 1(a) and (b), there were three main sunspots (one leading and two following) located in AR 11504. The negative sunspot in the southeast and the positive one in the west are labeled as N1 and P1, respectively. At ∼17:00 UT, a small δ sunspot was formed between N1 and P1 with two magnetic polarities as labeled with N2 and P2. The bottom panels in Figure 1 show further local high-resolution images, from which we can see that there was a light bridge inside the δ sunspot, the position corresponds to the magnetic interface between N2 and P2. In addition, for the filament we will analyze, the left end is rooted between the polarities N2 and P2. However, the magnetic polarity inversion line associated with the filament can only be clearly recognized in the δ sunspot.

Figure 2(a) illustrates the SXR light curves, showing the C1.0 flare and the C3.9 flare in 1–8 Å (red line) and 0.5–4 Å (magenta line). To investigate the evolution of radiation and magnetic flux for the δ sunspot during the filament eruption, we

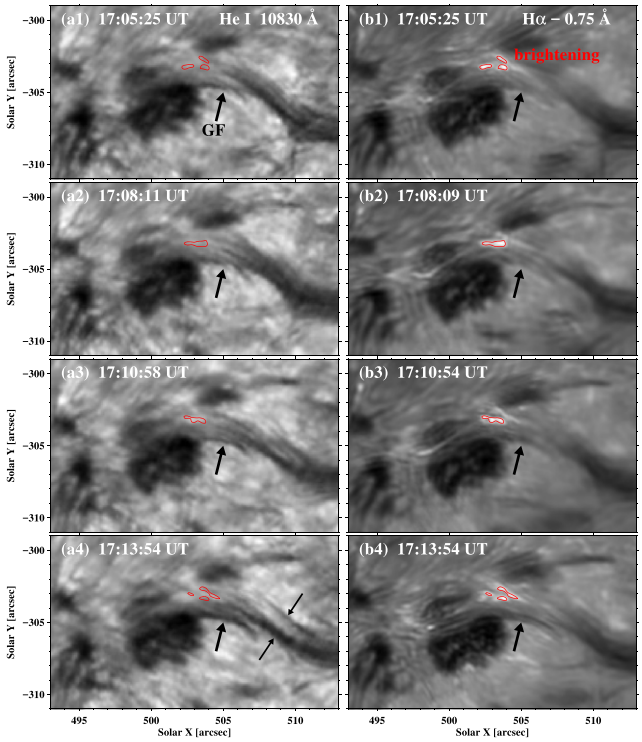

Figure 3. Growth process of the filament produced by magnetic reconnection. The left panels show four images in He I 10830 Å (a1)–(a4) and the right panels show four images in Hα blue wing (b1)–(b4). GF is pointed to by black thick arrows. The brightening near N2 is enclosed by red contours. The spitting threads are denoted by black thin arrows in panel (a4). An animation of the Hα blue wing (panels (b1)–(b4)) observations is available; it begins at 17:03 UT and ends on the same day at 17:16 UT. The animation real-time duration is 4 s and it shows continuous brightening near the eastern leg of the filament. The He I 10830 Å sequences are available in the top right portion of the animation available with Figure 2.

(An animation of this figure is available.)

calculated the total flux (normalized) of 10830 Å and TiO intensity, and the total positive and negative magnetic fluxes within the white box in Figure 1(e). Their temporal evolution is plotted in Figures 2(b) and (c). In particular, as can be seen from the red curve in Figure 2(b) for 10830 Å, the filament eruption underwent three processes: precursor, the first eruption, and the second eruption. The two eruptions corresponded to the two flares shown in Figure 2(a), first with the C1.0 flare at ∼17:27 UT, and then with the C3.9 flare at ∼17:39 UT. It is noteworthy that the radiation in 10830 Å had a slow increase including a small peak at ∼17:20 UT. Visual inspections of the movies of Hα images show continual brightening around the filament. From 17:05–17:25 UT, the TiO intensity continued to increase slowly, and the positive flux of the δ sunspot continued to decrease, while the negative flux began to decrease after the C1.0 flare, which indicates the occurrence of magnetic cancellation or reconnection before and during the first eruption.

3.2. The Precursor Phase

Figure 3 presents local high-resolution images for the δ sunspot before the precursor in 10830 Å (left panels) and Hα blue wing (right panels). At ∼17:03 UT, when we started to observing, there already was a growing filament (GF) near the footpoint of the filament, which is denoted by thick black arrows. The GF was gradually growing with continuous brightening closed to the eastern leg of the filament connected to N2, which is enclosed by red contours. Starting around 17:13 UT, the eastern leg of the filament began to bifurcate into two groups of fine threads, which is pointed to by two thin black arrows in Figure 3(a4). Until ∼17:24 UT, as shown in Figure 4(g), there were three groups of discernible threads, which are designated as Threads 1 (TH1), Threads 2 (TH2), and Threads 3 (TH3).

Figure 4 shows a cusp-type configuration formed between the filament and its adjoining loops (labeled Loop 1 in Figure 4(d)). Starting around 17:20 UT, the bright features, presumably plasmoid structures flowing along the filament and Loop 1 were detected in EUV bands, which are enclosed by the magenta ellipses in Figures 4(a)–(c). Almost simultaneously, a persistent reconnection point, which is marked by the magenta arrows in Figures 4(c) and (d), was observed at the interface between the filament and Loop 1 in 131 Å and 94 Å. The filament and Loop 1 were separately denoted by the black and yellow dotted lines in Figures 4(d) and (e). The corresponding magnetic fields are given in Figure 4(f). It is obvious that two footpoints of Loop 1 (labeled L1-FP1 and L1-FP2) were rooted in P2 and N1 while the filament was rooted in P1 and N2. In Figures 4(g) and (h), it can be seen that one footpoint of the GF was located at P2 (i.e., previous L1-FP1), while another footpoint was rooted in N2 (i.e., negative footpoint of the filament). In addition, an NLFFF extrapolation is performed to investigative the 3D magnetic fields in the source region, using the HMI vector magnetograms before eruptions (17:12 UT), and the extrapolated results are presented in the top and side view in Figure 5. Obviously, there are a flux rope (red lines) and a group of magnetic loop (yellow lines), which nearly correspond to the filament and Loop 1 in Figures 4(d) and (e), and their footpoints are consistent with those in the Figure 4(f).

3.3. The First Eruption

Figure 6 presents the process of the first eruption and the interaction between TH2 and its nearby magnetic structures. Starting at around 17:25 UT, the GF became unstable and erupted together with TH2, associated with a C1.0 class flare.

The erupting TH2 and the remaining TH3, as well as their footpoints, are marked with red arrows and letters in Figure 6(a2). The separated footpoints indicate that TH2 and TH3 have been completely splitted.

Subsequently, at ∼17:26 UT, the erupted GF was observed in the 94 Å (see Figures 6(c1) and (c2)), while another group of loops (labeled Loop 2) appeared, with two footpoints designated as L2-FP1 and L2-FP2. As shown in Figures 6(b) and (c), at the interface of TH2 and Loop 2, there is a continuous brightening in 94 Å and 131 Å and it is accompanied by the outflow along Loop 2. However, the outflow only appeared as an absorption feature in 10830 Å. These significant signals indicate that TH2 and Loop 2 underwent another magnetic reconnection. Of course, there is another possibility of merging or reconnection between different threads of the filaments, including TH2, GF, and F3 (presented in Figure 7(a)). It is worth noting that the GF was above the brightening feature, indicating that it is higher.

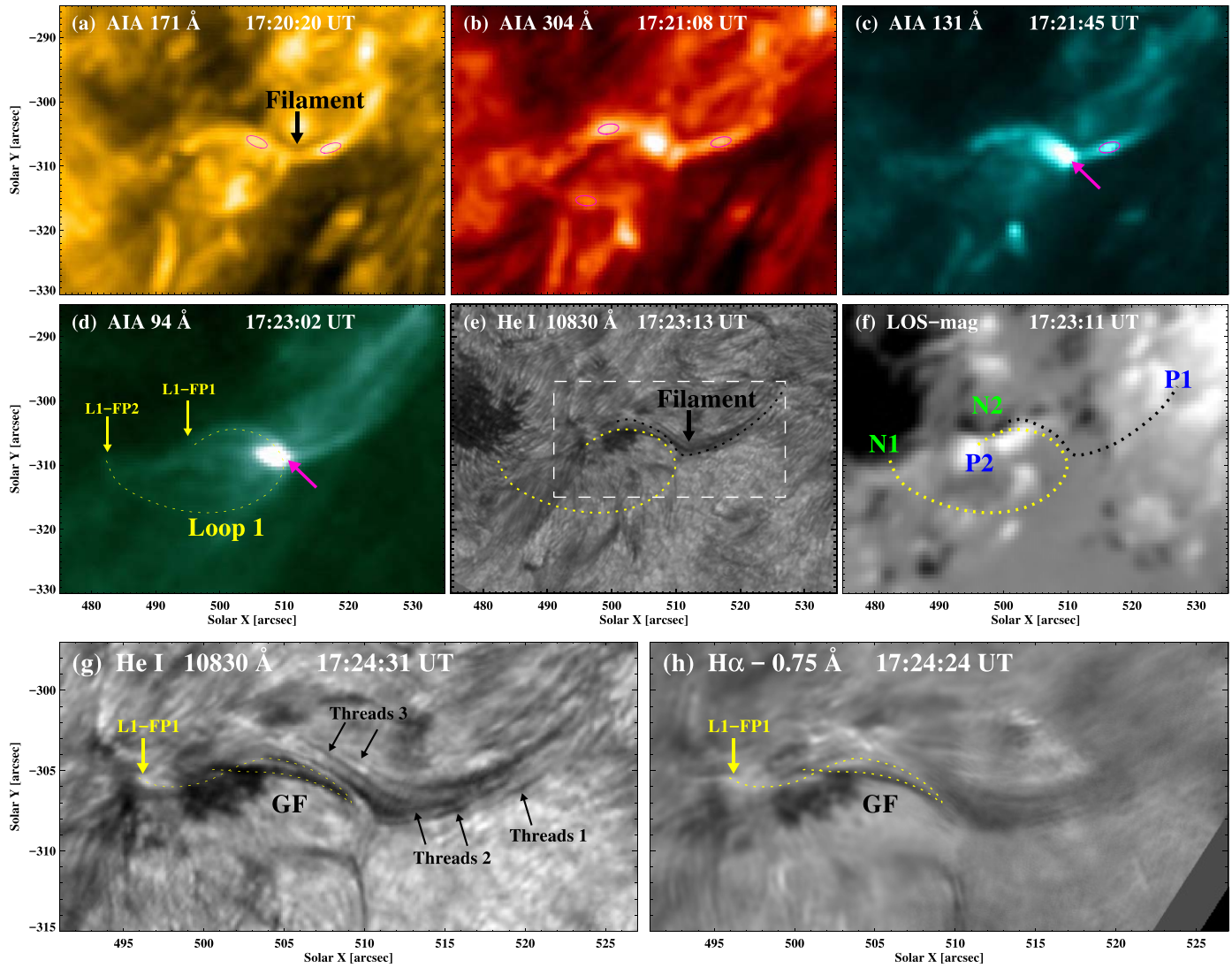

Figure 4. The cusp type formed between TH1 in the filament and Loop 1. Panels (a)–(d) show EUV images in 171 Å, 304 Å, 131 Å, and 94 Å. Panels (e) and (g) present two 10830 Å narrowband filtergrams, (f) an HMI LOS magnetogram and (h) an Hα blue wing image. The white rectangle in (e) shows the FOV of panels (g) and (h). The outflow and reconnection point are enclosed (pointed to) by the magenta ellipses (arrows) in panels (a)–(d). Loop 1 is outlined by yellow dashed lines in panels (d)–(f) and the two footpoints of Loop 1 (L1-FP1, L1-FP2) is pointed to by the yellow arrows in panels (d), (g), and h. TH1 is outlined by the black dashed lines in panels (e) and (f). The negative and positive magnetic fields are separately denoted by N1, N2, P1, and P2 in panel (f). The GF is outlined by the yellow dashed lines in panels (g) and (h). (An animation of the top six panels is available; it begins at 17:05 UT and ends the same day at 17:25 UT, lasting 5 s.)

(An animation of this figure is available.)

One distal end of the initial flare ribbon is pointed to by yellow arrows (L1-FP1) in Figure 6. Around 17:27 UT, the flare ribbon elongated to L2-FP1, and the radiation was significantly enhanced, corresponding to the peak in 10830 Å for the first eruption (see Figure 2(b)). Concurrently, there appeared an another brightening region of the flare ribbon, which is encircled in yellow circles in Figures 6(b3), (c3), and (d). The brightening region is found to be one footpoint of a hot channel formed after the eruption, while another footpoint is encircled with red circles. As shown in Figure 6(d1), both footpoints of the hot channel are rooted in the flare ribbon.

3.4. The Second Eruption

Figure 7 presents the process of the second eruption. From 17:31–17:34 UT, as shown in Figure 7(a), there was no significant brightening in 10830 Å and the Hα blue wing, corresponding to the valley between the first and second eruption on the 10830 Å time profile (see Figure 2(b)).

At about 17:31 UT, another filament (labeled F3) formed by the reconnection between Loop 1 and TH1 is detected in 10830 Å and the Hα blue wing, which is outlined by the yellow dashed line in Figures 7(a1) and (a3). The two footpoints of F3 are pointed to by yellow and red arrows, and corresponded to the previous L1-FP2 and positive footpoints of TH1, respectively. Similarly, a filament (labeled F4) was also detected in 10830 Å and the Hα blue wing, which is marked with cyan and red arrows in Figure 7(a). As described in the previous section, F4 may be formed by the reconnection between Loop 2 and TH2, and the possibility of the merging of different filaments cannot be excluded. Both F3 and F4 were unstable and erupted at ∼17:37 UT, associated with a C3.9 class flare and another weak CME as shown in Figure 8(a3).

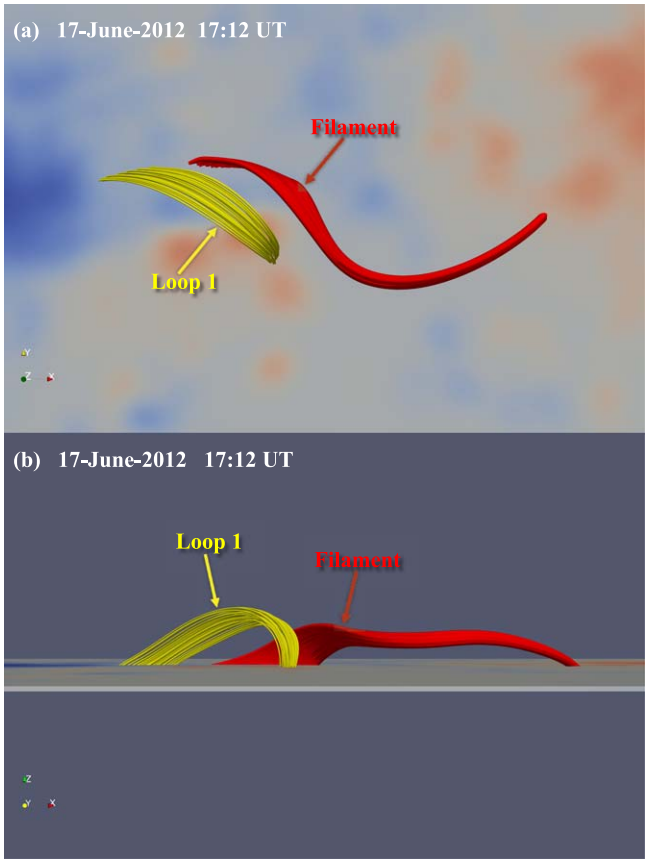

Figure 5. Top (top panel) and side (bottom panel) views of the NLFFF extrapolated filament (red) and Loop 1 (yellow) at 17:12 UT on 2012 June 17. The FOV of these panels is approximated from the FOV of Figure 4(f).

Figure 7(b) shows multiple initial brightenings shown as the flare ribbons and the remaining filament after two eruptions. Two distal ends of the initial flare ribbon are denoted by yellow arrows and circles. Particularly, the positive footpoint of F3 (pointed to by a red arrow) did not appear to be brightening in 10830 Å, but there was a significant brightening in the EUV bands. Similar to the first eruption, the footpoints of the hot channel formed during the second eruption were also rooted in the flare ribbon but in different regions, where the positive footpoint of F3 and the elongation region of the initial flare ribbon (enclosed by red circles) were. This suggested that multiple hot channels were formed by the two eruptions. At about 17:40 UT, the flare radiation reached its highest, corresponding to the curve peak for the second eruption in 10830 Å (see Figure 2(b)). The post-flare loops are outlined by the black contours in Figures 7(c2) and (c3).

4. Interpretation and Discussion

Based on the observation, schematic diagrams showing the evolution of the partial eruption are provided in Figure 9. As shown in the enlarged partial diagram in Figure 9(a), Loop 1 was composed of thin magnetic field lines, while the filament was composed of fine threads. The group of threads that reconnected with Loop 1 is marked as TH1, which can be observed in Figure 4(g). When Loop 1 and the filament approached each other, the magnetic reconnection started. The magnetic lines in Loop 1 and the threads of the filament were disconnected at the position marked by the asterisk. Then the eastern part of TH1 reconnected to the western leg of Loop 1, forming the GF, while the western part of TH1 reconnected to the eastern leg of Loop 1, forming another new filament F3. The continuous accumulation of new magnetic lines corresponds to the progressive growth of the GF. Apart from TH1, the remaining threads in the filament split into two groups (i.e., TH2 and TH3) vertically during the reconnection between TH1 and Loop 1. Then, the GF erupted together with TH2. Magnetic reconnection taking place between the erupting TH2 and Loop 2, or the merging interaction between different threads of the filaments, produced another unstable filament F4, although only the former case is shown here. Finally, F3 and F4 erupted together and TH3 remained. As shown in Figure 8, the associated weak outflow was detected by LASCO/C2.

The three-step eruptions we report here have hardly been reported before. Earlier, multi-step eruptions occurred when a filament experienced a failed eruption and then erupted successfully, and the interval between eruptions was at least 1 hr or longer (Byrne et al. 2014; Gosain et al. 2016; Chandra et al. 2017). Filippov (2018) proposed the existence of two critical heights as a result of the non-monotonic coronal magnetic field. Therefore, we presume that such critical heights should also exist for the active region here; this may explain why F3 did not erupt with the GF together, but only with F4 after the subsequent interaction.

In this study, the filament and its nearby loops (Loop 1 and Loop 2) were rooted in the same δ sunspot. Figure 10 presents the vector magnetic fields of the δ sunspot region, which originate from the negative and positive vertical fields. Obviously, the magnetic fields in the δ sunspot region were more compact with opposite polarities, which were further identified as high-gradient, strongly sheared, and non-potential (Hagyard et al. 1984; Tanaka 1991; Schrijver 2007). Such non-potential fields tend to produce magnetic reconnections and eruptions in the case of photospheric motion (Fang & Fan 2015; Liu et al. 2021). Hence, the filament and its nearby loops were favored configurations for the magnetic reconnections and eruptions. In this case, the reconnection of the filament (TH2) and its nearby loops (Loop 2) may still be occurring during the first eruption. However, the observation is not very clear from the present images. Therefore, the continuous brightening during the first eruption in 131 Å and 94 Å could also result from the merging of TH2, GF, and F3 in the favored magnetic configurations (Schmieder et al. 2004; DeVore et al. 2005; Chandra et al. 2011; Török et al. 2011).

Usually, the precursors of brightening prior to filament eruptions are closely related to the triggering mechanism for eruptions. Typically, transient X-ray brightenings, so-called preflares, are observed before the flares (Chifor et al. 2007; Sterling et al. 2011), which are coincident with magnetic cancellation or emerging magnetic flux (Schmieder et al. 2008). Moreover, Yan et al. (2013) suggested that the brightening in the chromosphere before the filament expansion may indicate the onset of TC reconnection. And Chen et al. (2018) detected obvious brightenings in UV bands and hot outflows in the chromosphere, which showed the preflare reconnection process of the partial eruptions. Similarly, we also found continuous chromosphere brightening near the footpoint of the filament and magnetic cancellation during the growth of the GF. Therefore, we believe that the magnetic reconnection between the filament and Loop 1 has already begun when the GF appears. The magnetic reconnection continued until the

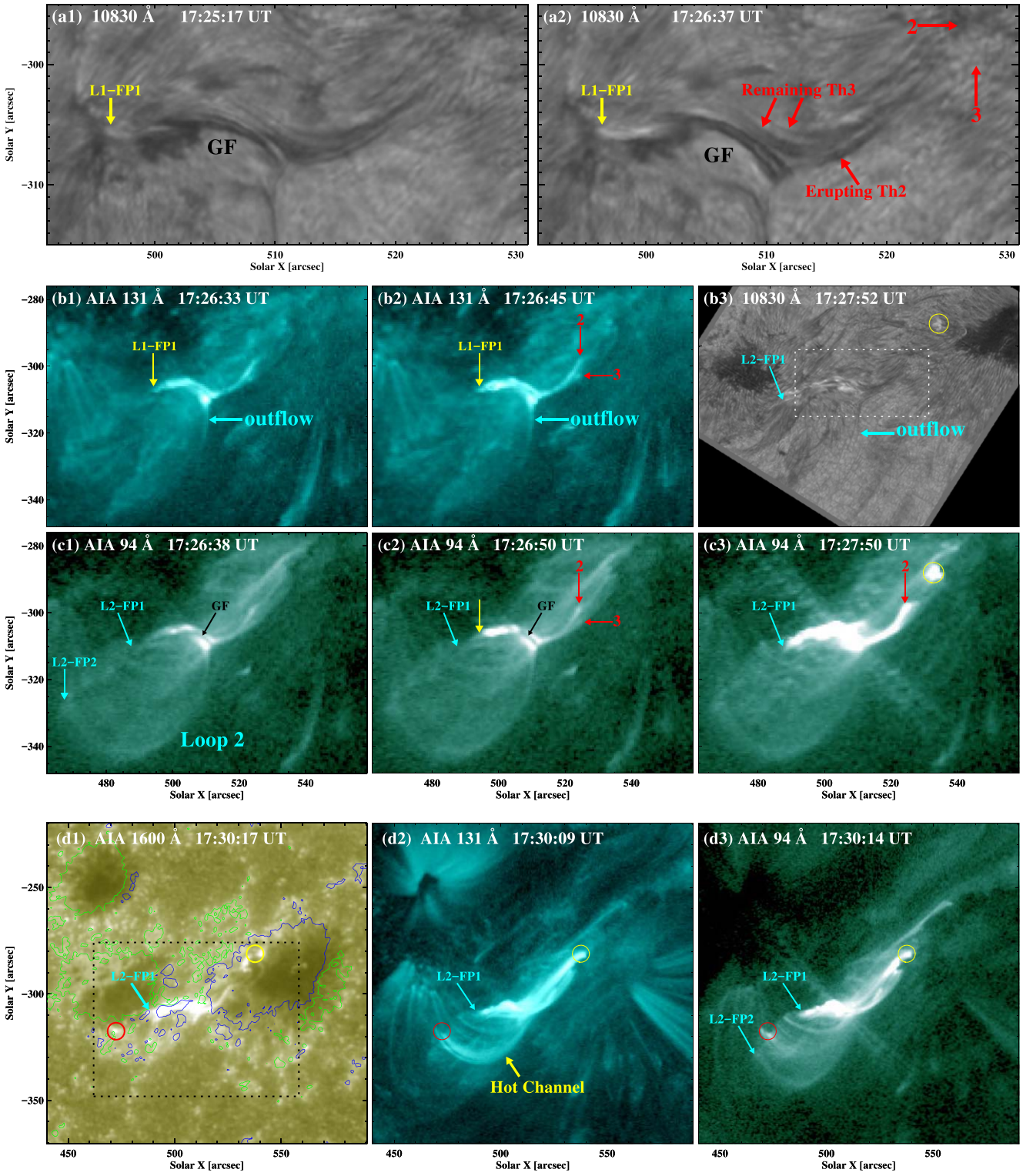

Figure 6. The process of the first eruption and the interaction between TH2 and its nearby magnetic structures. Panels (a1), (a2), and (b3) present three 10830 Å narrowband filtergrams and the other panels show images in AIA 131 (Å) ((b1), (b2), and (d2)), 94 Å ((c1), (c3), and (d3)) and 1600 Å (d1). The white dashed rectangle in (b3) shows the FOV of (a1) and (a2) and the black dashed rectangle in (d1) shows the FOV of (b) and (c). The GF is marked with black letters and arrows in panels (a)–(c). The erupting TH2 and remaining TH3 are pointed to by red arrows in (a2). The footpoints of the erupting TH2 and remaining TH3 are separately marked with red letters 2 and 3 in panels (a)–(c). The outflow between TH2 and Loop 2 is marked with cyan thick arrows in panels (b1)–(b3). The two footpoints of the Loop 2 (L2-FP1, L2-FP2) are marked with cyan thin arrows in (b3), (c1)–(c3), and (d1–d3). The yellow and red circles in (b3), (c3), and (d1)–(d3) enclose the initial flares. The green and blue contours in (d1) are the same as those in Figure 1. (An animation of panels (b) and (c) is available; it begins at 17:25 UT and ends on the same day at 17:30 UT, lasting 6 s, which shows the first eruption.)

(An animation of this figure is available.)

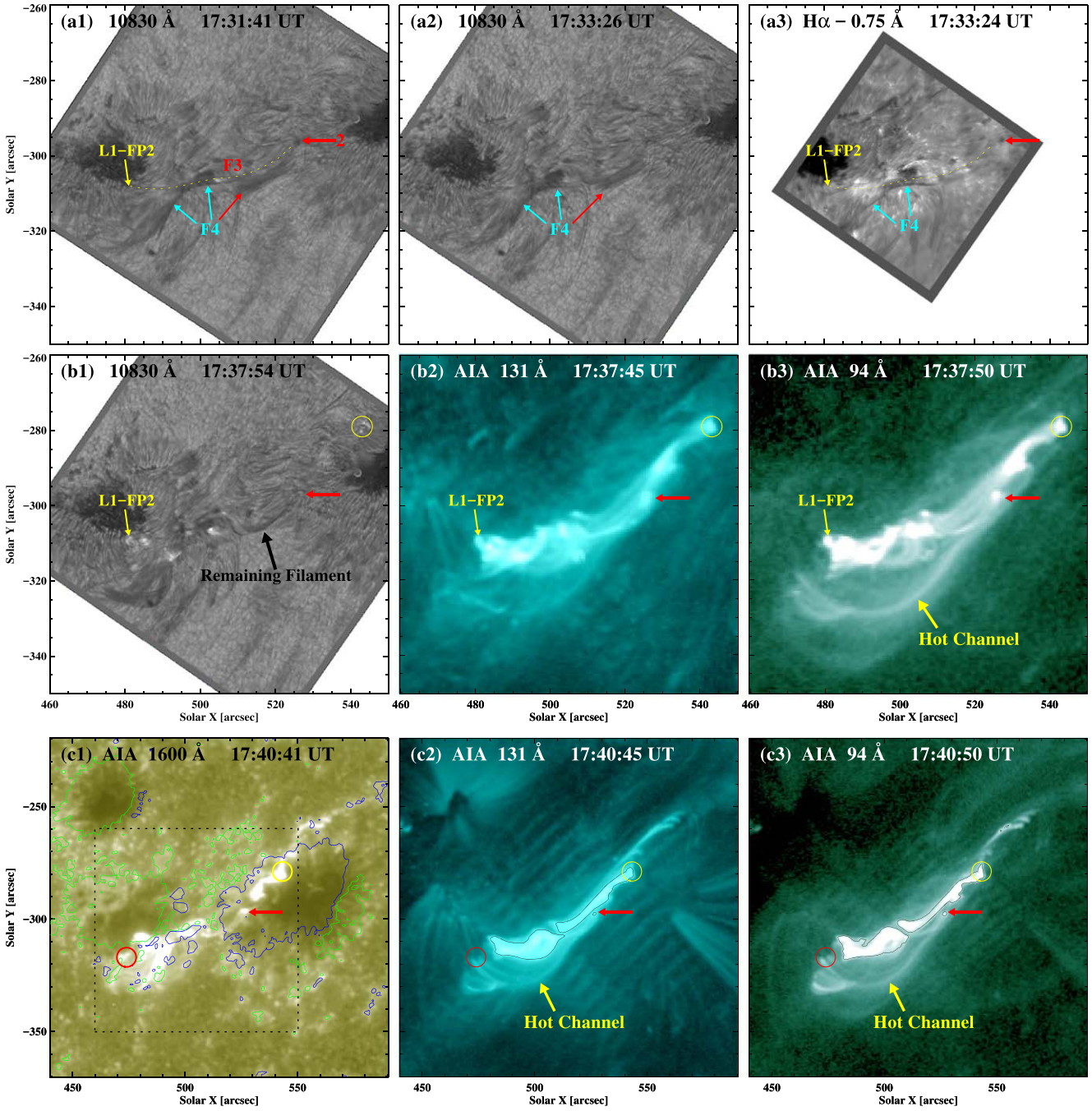

Figure 7. The process of the second eruption. Panels (a1), (a2), and (b1) show three 10830 Å narrowband filtergrams and panel (a3) shows an Hα blue wing image. The other panels show images in AIA 131 Å ((b2) and (c2)), 94 Å ((b3) and (c3)), and 1600 Å (c1). The black dashed rectangle in (c1) shows the FOV of (a) and (b). F3 is outlined by the yellow dashed lines while the cyan and red thin arrows in (a) point to F4. The footpoints of F3 (i.e., the footpoint of erupting TH2 and L1-FP2) are separately marked with red thick arrows and yellow thin arrows in (a)–(c). The initial flares are enclosed by yellow and red circles in (b) and (c). The green and blue contours in (c1) is same as that in Figure 1. The black contours in (c2) and (c3) outline the post-flare loops. (An animation of panels (b1)–(b3) is available; it begins at 17:30 UT and ends on the same day at 17:55 UT, lasting 6 s, which shows the second eruption.)

(An animation of this figure is available.)

brightening plasmoids and reconnection point appeared in EUV bands. We support that the reconnection process was a transition from the low corona to the high corona; hence, no characteristic signals in EUV bands was detected at the beginning.

Generally, the splitting is mostly caused by internal magnetic reconnection (Gibson & Fan 2006), which tends to take place in the case of shearing motion or the so-called filament-hosting flux rope (Cheng et al. 2018). However, Chen et al. (2018) present a three-part splitting due to TC reconnection below the filament and Zheng et al. (2019) highlighted the role of the TC reconnection between the overlying sheared loops. Meanwhile, Monga et al. (2021) proposed that the reconnection between a filament and its nearby EUV loops could induce the vertical

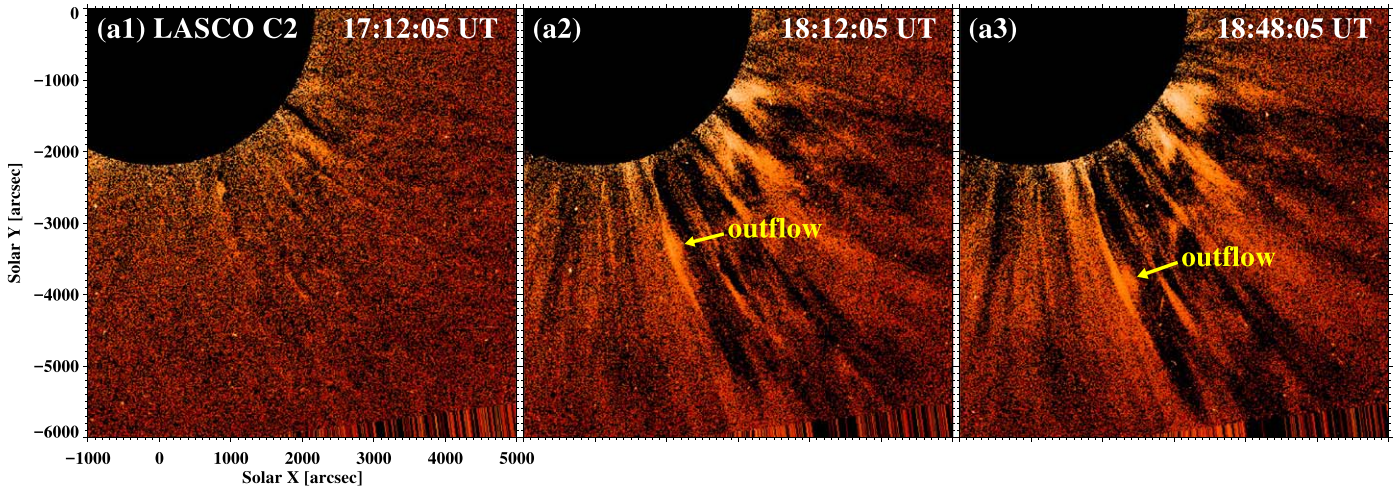

Figure 8. Three snapshots of the white-light CME observed by LASCO/C2. (An animation of this figure is available; it begins at 17:12 UT and ends on the same day at 19:48 UT, lasting 3 s.)

(An animation of this figure is available.)

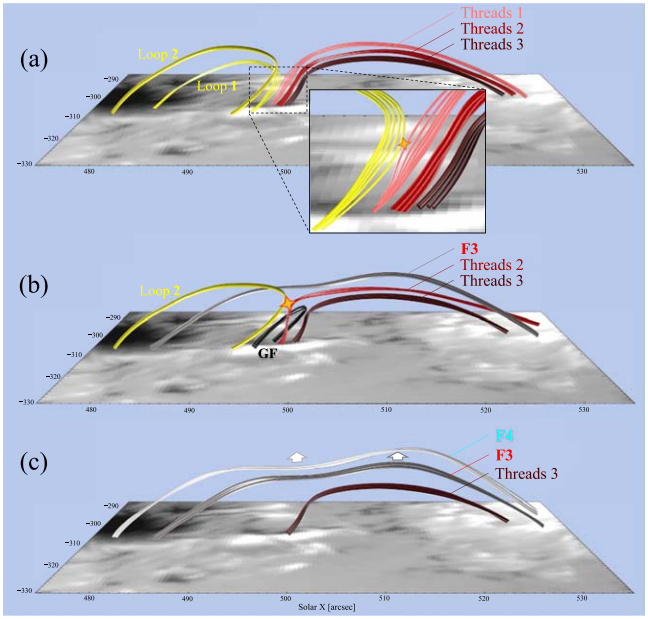

Figure 9. Schematic diagrams showing the scenario of vertical splitting in the partial eruption. The yellow lines in panels (a) and (b) represent Loop 1 and Loop 2. The red lines with different color depths represent the threads of the filament. The black, dark gray, and light gray lines separately represent GF, F3, and F4. The reconnection sites are denoted by star symbols.

splitting through destabilizing the magnetic topology of the filament; hence, we believe that the splitting found in our observation was also caused by a similar external magnetic reconnection. Such interaction during the reconnection may be the transfer of magnetic flux between the filament and its nearby loops (Kliem et al. 2014). Thus, we support that the eruption of TH2 was due to the magnetic flux injection from Loop 1. In conclusion, magnetic reconnection between a filament and its nearby loops could induce the splitting and partial eruption of the filament.

In addition, although the footpoints of the hot channels produced during two eruptions were root in the flare ribbon, but they were not identical, which implied the existence of multiple hot channels and suggested that the formation of hot channels was closely associated with flares. The hot channels in this event are consistent with the characteristics summarized by Cheng & Ding (2016), i.e., EUV brightening structures with the high temperature rooted in the penumbra or penumbra edge. However, the hot channels here are not sigmoidal but arcaded.

5. Summary

In this paper, we reported a three-step partial eruption of an active filament observed by GST in AR 11504 on 2012 July 17. With the help of high-resolution imaging at 10830 Å, we directly observed the vertical splitting process. Combined with the multiwavelength data from SDO/AIA and HMI, we investigated the detailed process of the precursor and two successive eruptions. We confirm that the vertical splitting and partial eruptions were induced by the magnetic reconnection between the filament and its nearby loops, which is the so-called external magnetic reconnection. Its initial stage went on gently, giving rise to the slowly growing filament and the slowly rising brightening, which constitute the precursor phase of the partial eruptions. Such a precursor was totally missed in the GOES light curves. In conclusion, such a kind of external magnetic reconnection should be a potential triggering mechanism for partial filament eruptions.

The authors thank Dr. Yijun Hou of the National Astronomical Observatory for constructive suggestions. SDO is a mission of NASA's Living With a Star Program. AIA and HMI data are courtesy of the NASA/SDO science teams. The BBSO operation is supported by NJIT and US NSF AGS 1821294 grant. The operation of GST is partly supported by the Korea Astronomy and Space Science Institute, the Seoul National University, and the Key Laboratory of Solar Activities of the Chinese Academy of Sciences (CAS) and the Operation, Maintenance and Upgrading Fund of CAS for Astronomical Telescopes and Facility Instruments. Y.W. is supported by the Youth Fund of Jiangsu (No. BK20191108). Q.M.Z. is supported by the CAS Key Laboratory of Solar Activity, National Astronomical Observatories (KLSA202006), and the International Cooperation and Interchange Program (11961131002). This work is supported by the National Natural Science Foundation of China grant Nos. 41761134088, 11790302 (11790300), 12073042, 12003072,

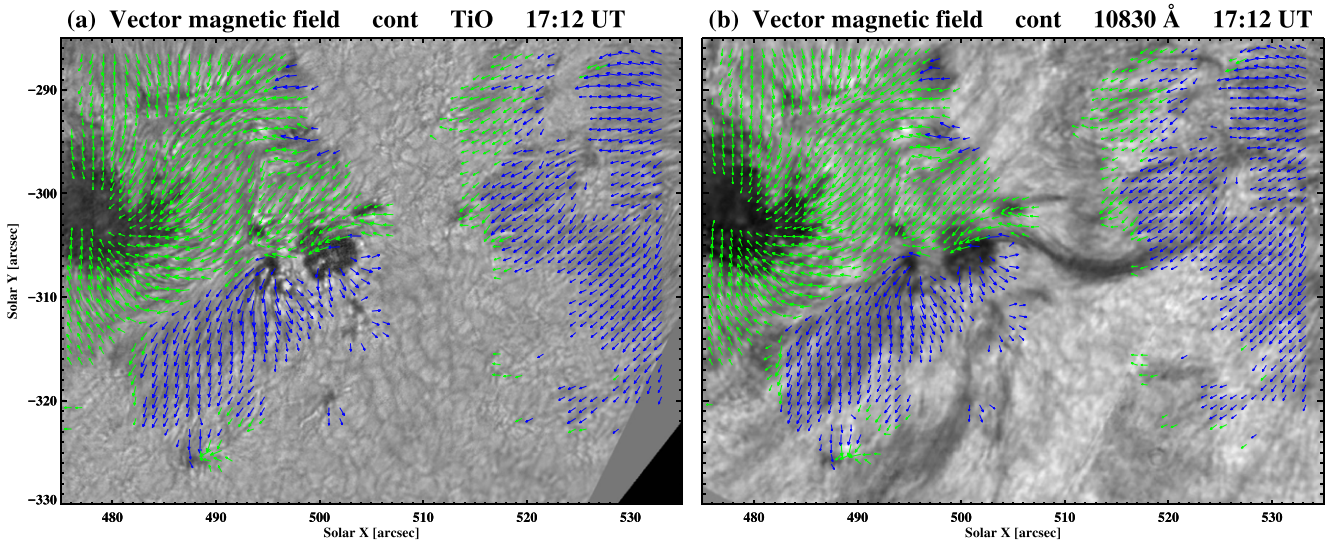

Figure 10. Horizontal magnetic fields, which originate from the areas of the negative and positive vertical magnetic fields, are separately depicted by green and blue arrows, and overlaid on the simultaneous TiO and 10830 Å images at 17:12 UT.

11773079, 11473071, and U1731241 as well as the Strategic Priority Research Program on Space Science, CAS, grant Nos. XDA15052200 and XDA15320301.

ORCID iDs

Jun Dai https://orcid.org/0000-0003-4787-5026
Zhentong Li https://orcid.org/0000-0002-4230-2520
Ya Wang https://orcid.org/0000-0003-3699-4986
Zhe Xu https://orcid.org/0000-0002-9121-9686
Leping Li https://orcid.org/0000-0001-5776-056X
Qingmin Zhang https://orcid.org/0000-0003-4078-2265
Yingna Su https://orcid.org/0000-0001-9647-2149
Haisheng Ji https://orcid.org/0000-0002-5898-2284

References

Alexander, D., Liu, R., & Gilbert, H. R. 2006, ApJ, 653, 719
Berger, T. 2014, in IAU Symp. 300, Nature of Prominences and their Role in Space Weather, Vol. 300, ed. B. Schmieder, J.-M. Malherbe, & S.-T. Wu (Cambridge: Cambridge Univ. Press) 15
Berger, T. E., & Haerendel, G. 2009, AGU Fall Meeting Abstracts, SH44A-07
Bi, Y., Jiang, Y., Yang, J., et al. 2015, ApJ, 805, 48
Birn, J., Forbes, T. G., & Hesse, M. 2006, ApJ, 645, 732
Brueckner, G. E., Howard, R. A., Koomen, M. J., et al. 1995, SoPh, 162, 357
Byrne, J. P., Morgan, H., Seaton, D. B., et al. 2014, SoPh, 289, 4545
Cao, W., Coulter, R., Gorceix, N., et al. 2010, Proc. SPIE, 7742, 774220
Cao, W., Gorceix, N., Coulter, R., et al. 2010, AN, 331, 636
Chae, J., Denker, C., Spirock, T. J., et al. 2000, SoPh, 195, 333
Chandra, R., Filippov, B., Joshi, R., et al. 2017, SoPh, 292, 81
Chandra, R., Schmieder, B., Mandrini, C. H., et al. 2011, SoPh, 269, 83
Chen, H., Duan, Y., Yang, J., et al. 2018, ApJ, 869, 78
Chen, J. 1996, JGR, 101, 27499
Chen, P. F. 2011, LRSP, 8, 1
Chen, P. F., Innes, D. E., & Solanki, S. K. 2008, A&A, 484, 487
Chen, P. F., & Shibata, K. 2000, ApJ, 545, 524
Cheng, X., & Ding, M. D. 2016, ApJS, 225, 16
Cheng, X., Kliem, B., & Ding, M. D. 2018, ApJ, 856, 48
Chifor, C., Tripathi, D., Mason, H. E., et al. 2007, A&A, 472, 967
Dai, J., Ji, H., Li, L., et al. 2021, ApJ, 906, 66
Dai, J., Yang, J., Li, L., et al. 2018, ApJ, 869, 118
Devi, P., Joshi, B., Chandra, R., et al. 2020, SoPh, 295, 75
DeVore, C. R., Antiochos, S. K., & Aulanier, G. 2005, ApJ, 629, 1122
Engvold, O. 1998, IAU Colloq 167: New Perspectives on Solar Prominences, 150 (Cambridge: Cambridge Univ. Press), 23
Engvold, O. 2015, Solar Prominences, 415 (Cham: Springer), 31
Fang, F., & Fan, Y. 2015, ApJ, 806, 79
Feynman, J., & Martin, S. F. 1995, JGR, 100, 3355
Filippov, B. 2018, MNRAS, 475, 1646
Gibson, S. E. 2018, LRSP, 15, 7
Gibson, S. E., & Fan, Y. 2006, ApJL, 637, L65
Gilbert, H. R., Alexander, D., & Liu, R. 2007, SoPh, 245, 287
Gilbert, H. R., Holzer, T. E., Burkepile, J. T., et al. 2000, ApJ, 537, 503
Gilbert, H. R., Holzer, T. E., & Burkepile, J. T. 2001, ApJ, 549, 1221
Goode, P. R., Coulter, R., Gorceix, N., et al. 2010, AN, 331, 620
Gosain, S., Filippov, B., Ajor Maurya, R., et al. 2016, ApJ, 821, 85
Guo, Y., Xia, C., & Keppens, R. 2016, ApJ, 828, 83
Haerendel, G., & Berger, T. 2011, ApJ, 731, 82
Hagyard, M. J., Smith, J. B., Teuber, D., et al. 1984, SoPh, 91, 115
Hernandez-Perez, A., Su, Y., Veronig, A. M., et al. 2019, ApJ, 874, 122
Hood, A. W., & Priest, E. R. 1981, GApFD, 17, 297
Ji, H., Wang, H., Schmahl, E. J., et al. 2003, ApJL, 595, L135
Ji, K., Liu, H., Jin, Z., Shang, Z., & Qiang, Z. 2019, ChSBu, 2019.64, 1738
Karpen, J. T. 2015, Solar Prominences, 415 (Cham: Springer), 237
Keppens, R., Meliani, Z., van Marle, A. J., et al. 2012, JCoPh, 231, 718
Keppens, R., Nool, M., Tóth, G., et al. 2003, CoPhC, 153, 317
Kliem, B., & Török, T. 2006, PhRvL, 96, 255002
Kliem, B., Török, T., Titov, V. S., et al. 2014, ApJ, 792, 107
Labrosse, N., Heinzel, P., Vial, J.-C., et al. 2010, SSRv, 151, 243
Lemen, J., Title, A., Akin, D., et al. 2012, SoPh, 275, 17
Li, L., Zhang, J., Peter, H., et al. 2016, NatPh, 12, 847
Lin, Y., Engvold, O., Martin, S., et al. 2008, AGUSM, SH23A-05
Lin, Y., Engvold, O., Rouppe van der Voort, L., et al. 2005, SoPh, 226, 239
Liu, L., Liu, J., Chen, J., et al. 2021, A&A, 648, A106
Liu, R., Alexander, D., & Gilbert, H. R. 2007, ApJ, 661, 1260
Liu, R., Kliem, B., Török, T., et al. 2012, ApJ, 756, 59
Liu, Y., Su, J., Xu, Z., et al. 2009, ApJL, 696, L70
Mackay, D. H., Karpen, J. T., Ballester, J. L., et al. 2010, SSRv, 151, 333
Martin, S. F. 1980, SoPh, 68, 217
Martin, S. F. 1998, SoPh, 182, 107
Mitra, P. K., Joshi, B., & Prasad, A. 2020, SoPh, 295, 29
Monga, A., Sharma, R., Liu, J., et al. 2021, MNRAS, 500, 684
Moore, R. L., Sterling, A. C., Hudson, H. S., et al. 2001, ApJ, 552, 833
Okamoto, T. J., Tsuneta, S., Berger, T. E., et al. 2007, Sci, 318, 1577
Pan, H., Liu, R., Gou, T., et al. 2021, ApJ, 909, 32
Parenti, S. 2014, LRSP, 11, 1
Pesnell, W., Thompson, B., & Chamberlin, P. 2012, SoPh, 275, 3
Porth, O., Xia, C., Hendrix, T., et al. 2014, ApJS, 214, 4
Régnier, S., Walsh, R. W., & Alexander, C. E. 2011, A&A, 533, L1
Schmieder, B., Chandra, R., Berlicki, A., et al. 2010, A&A, 514, A68
Schmieder, B., Mein, N., Deng, Y., et al. 2004, SoPh, 223, 119
Schmieder, B., Török, T., & Aulanier, G. 2008, in AIP Conf. Ser. 1043, Exploring the Solar System and the Universe, 1043(Melville, NY: AIP), 260

Schou, J., Scherrer, P., Bush, R., et al. 2012, SoPh, 275, 229
Schrijver, C. J. 2007, ApJL, 655, L117
Shen, Y., Liu, Y., & Su, J. 2012, ApJ, 750, 12
Shen, Y.-D., Liu, Y., & Liu, R. 2011, RAA, 11, 594
Sterling, A. C., & Moore, R. L. 2005, ApJ, 630, 1148
Sterling, A. C., Moore, R. L., & Freeland, S. L. 2011, ApJL, 731, L3
Tanaka, K. 1991, SoPh, 136, 133
Török, T., Chandra, R., Pariat, E., et al. 2011, ApJ, 728, 65
Török, T., & Kliem, B. 2005, ApJL, 630, L97
Török, T., Kliem, B., & Titov, V. S. 2004, A&A, 413, L27
Tripathi, D., Gibson, S. E., Qiu, J., et al. 2009, A&A, 498, 295
Tripathi, D., Reeves, K. K., Gibson, S. E., et al. 2013, ApJ, 778, 142
Turmon, M., Jones, H. P., Malanushenko, O. V., et al. 2010, SoPh, 262, 277
van Ballegooijen, A. A., & Martens, P. C. H. 1989, ApJ, 343, 971
Wang, Y., Ji, H., Warmuth, A., et al. 2020, ApJ, 905, 126
Wang, Y., Su, Y., Shen, J., et al. 2018, ApJ, 859, 148
Wiegelmann, T., Inhester, B., & Sakurai, T. 2006, SoPh, 233, 215
Wiegelmann, T., Thalmann, J. K., Inhester, B., et al. 2012, SoPh, 281, 37
Xue, Z., Yan, X., Cheng, X., et al. 2016, NatCo, 7, 11837
Yan, X. L., Qu, Z. Q., Kong, D. F., et al. 2013, A&A, 557, A108
Yang, J., Hong, J., Li, H., et al. 2020, ApJ, 900, 158
Zeng, Z., Qiu, J., Cao, W., et al. 2014, ApJ, 793, 87
Zhang, Q. M., Chen, P. F., Xia, C., et al. 2012, A&A, 542, A52
Zhang, Q. M., Ning, Z. J., Guo, Y., et al. 2015, ApJ, 805, 4
Zheng, R., Yang, S., Rao, C., et al. 2019, ApJ, 875, 71
Zheng, R., Zhang, Q., Chen, Y., et al. 2017, ApJ, 836, 160